

Enhanced Electrochemical Performance Ru³⁺ Doped Li₂FeP₂O₇ as Cathode for Lithium Ion Batteries

Hee-Won Jung, Seong-Hun Lee, Kwang-Sun Ryu*

Department of Chemistry, University of Ulsan, Ulsan 680-749, Korea

*E-mail: ryuks@ulsan.ac.kr

Received: 19 June 2018 / Accepted: 18 August 2018 / Published: 5 November 2018

Li₂Fe_{1-x}Ru_xP₂O₇ (x = 0, 0.005, 0.01, 0.02, 0.03, and 0.04) were prepared by a simple sol-gel synthesis method. Detailed lattice information, including the observation of a monoclinic P21/c (14) space group and crystal structure, was determined using XRD with rietveld refinement. To further confirm the oxidation and chemical states of elements within the samples, XPS measurements of each element are used. The electrochemical measurements were conducted using EIS, CV, and galvanostatic charge-discharge testing. Li₂Fe_{0.99}Ru_{0.01}P₂O₇ exhibited an increased specific discharge capacity of 100.22mAh/g at 0.05C and decreased polarization during charge and discharge. Li₂Fe_{0.99}Ru_{0.01}P₂O₇ exhibited the best rate-capabilities at various current densities, as well as the best cycle abilities in the voltage range of 2.0-4.5V. Fe K-edge and Ru K-edge in-situ XAS were carried out for samples of Li₂FeP₂O₇ and Li₂Fe_{0.99}Ru_{0.01}P₂O₇ in order to observe changes in the structures of the materials during electrochemical reaction. The results indicate that the structural rearrangement of Li₂Fe_{0.99}Ru_{0.01}P₂O₇ might be reduced by the slight shrinkage of the lattice due to the “pillar effects” of Ru³⁺. Also, Li₂Fe_{0.99}Ru_{0.01}P₂O₇ demonstrated higher electronic conductivity and ionic diffusion coefficient than Li₂FeP₂O₇. Therefore, the higher electrochemical performance of Li₂Fe_{0.99}Ru_{0.01}P₂O₇ was related with structure stability, electronic conductivity, and ionic diffusion coefficient.

Keywords: Lithium ion batteries, Cathode, Lithium iron pyrophosphate, Ru-doping, pillar effect

1. INTRODUCTION

Lithium metal oxides, utilizing a range of transition metals (LiMO₂, M = transition metal) have been widely used as cathode materials for lithium ion batteries. The increasing demand for these batteries due to their broadening applications within electronic devices has brought issues of cost and safety to the fore. Although several other cathode materials, including LiFePO₄ [1, 2] and polyanion-based compounds, such as phosphates (PO₄)³⁻, silicates (SiO₄)⁴⁻, and borates (BO₃)³⁻, have been

considered as next generation materials [3-4]. Nishimura et al. first reported the application of $\text{Li}_2\text{FeP}_2\text{O}_7$, which exhibits the highest reversible potential of 3.5V (vs. Li/Li^+) among all Fe-containing phosphate based cathodes, as well as a 2D lithium ion diffusion pathway in the b and c plane. Its specific discharge capacity is 110mAh/g at 2.0V-4.5V (vs. Li/Li^+) [5]. The primary advantage of polyanionic phosphate materials such as $(\text{PO}_4)^{3-}$, $(\text{P}_2\text{O}_7)^{4-}$, and $(\text{P}_3\text{O}_{10})^{5-}$ are their thermal stability and relative safety [6-9].

On the other hand, $\text{Li}_2\text{FeP}_2\text{O}_7$ generally exhibits poor rate capability and theoretical discharge capacities due to its poor electronic and ionic conductivity [10, 11]. Several strategies have been investigated in order to overcome the electrochemical performance limitations of $\text{Li}_2\text{FeP}_2\text{O}_7$ cathode materials, including nanosizing [12], surface carbon coating [13-15], and cation doping in iron sites with materials such as Mg [16], V [17], Mn [16, 18], Co [18], and Ni [19].

Until now, there has been no reported study of the substitution of iron atoms by ruthenium atoms. In this study, we synthesized a $\text{Li}_2\text{Fe}_{1-x}\text{Ru}_x\text{P}_2\text{O}_7$ ($x = 0, 0.005, 0.01, 0.02, 0.03, \text{ and } 0.04$) cathode using the sol-gel method to improve the electrochemical performance as reduced structural distortion. Ru doping brings the crystal structural stability as pillar effects. That property was to be investigated through studies with synchrotron, electronic conductivity and diffusion coefficient

2. EXPERIMENTAL

2.1. Materials synthesis

The monoclinic $\text{Li}_2\text{FeP}_2\text{O}_7$ powders were prepared through the following method. Stoichiometric amounts of LiH_2PO_4 (Sigma-aldrich, 99%), $\text{Fe}(\text{COOCH}_3)_2$ (alfa, 99.6%), as well as sucrose as the carbon source were used as the starting materials for the sol-gel reaction. LiH_2PO_4 has been determined through previous studies as the best lithium sources for the synthesis of $\text{Li}_2\text{FeP}_2\text{O}_7$ [20-21, 25], as lithium and phosphorous are present in the same equivalent ratio of atoms, reducing the generation of side products and increasing the volume of the desired final product. The starting materials were mixed in an appropriate amount of de-ionized water. The solutions were by stirred for 30 min, after which citric acid was added. Citric acid was used as both reducing and chelating agents in the preparation of the gel. The solvent was evaporated and dried at 80 °C in an oven overnight. The viscous resin which remained after the evaporation of the solvent is thought to occur due to the formation of a chemical bond between the carboxylic acid groups present in the complexing agent and the metal ions [26]. The mixture was then calcined in a tube furnace at 650 °C for 12 h under flowing argon gas, and was cooled to room temperature in the tube furnace under the same Ar flow.

$\text{Li}_2\text{Fe}_{1-x}\text{Ru}_x\text{P}_2\text{O}_7$ ($x = 0, 0.005, 0.01, 0.02, 0.03, \text{ and } 0.04$) were prepared using the above procedure, with the addition of various quantities of RuCl_3 (Sigma-aldrich, 99.98%) to doped samples. In order to prepare $\text{Li}_2\text{Fe}_{1-x}\text{Ru}_x\text{P}_2\text{O}_7$ ($x = 0.005, 0.01, 0.02, 0.03, \text{ and } 0.04$), LiH_2PO_4 , $\text{Fe}(\text{COOCH}_3)_2$, and RuCl_3 were mixed in a molar ratio of 2:1-x:x, respectively.

2.2. Characterization

High resolution synchrotron X-ray powder diffraction (HRPD) measurements were carried out at Pohang Light Source-II. The samples were scanned from 10 to 125.5° with step size of 0.01°. The incident X-rays were vertically collimated using a mirror and were monochromatized to a wavelength of 1.5475 Å using a double-crystal Si (111) monochromator. X-ray photoelectron spectroscopy (XPS) was carried out using an ESCALAB 250Xi spectrometer (Thermo Scientific, USA) equipped with monochromic Al K α radiation (1486.6 eV). Field emission scanning electron microscopy (FE-SEM) was carried out using a JSM-6500F microscope (JEOL, Japan). Transmission electron microscopy (HR-TEM) was carried out using a JEM-2100F microscope (JEOL, Japan) with an accelerating voltage of 200 kV.

Electrochemical characterizations were conducted using CR-2032 type coin cells. The electrode consisted of the active material, super-P and polyvinylidene fluoride 5130 (PVdF5130) in an 8:1:1 ratio, to which *N*-methyl pyrrolidinone was added until a viscous slurry was formed. The slurries were pasted on the aluminum current collector and were then dried at 80 °C for 12 h. The half-cell was prepared using the positive electrode and lithium foil (0.3mm) and the negative electrode, which were separated by separator with polypropylene film, and 1 M LiPF₆ EC and DMC in a ratio of 1:2, in 2.0% VC as the electrolyte. Galvano-static charge-discharge cycling was performed from 0.05C to 5C with cut-off voltages of 2.0-4.5 V (vs. Li/Li⁺) at room temperature. Cyclic voltammetry was carried out using a WBCS3000 battery cycler (WonAtech, Korea). Electrochemical impedance spectra and ionic diffusion measurements were carried out using a SP-300 electrochemical analyzer (Biologic, France).

In situ X-ray absorption spectra (XAS) were determined at the Fe K-edge in transmission mode and at the Ru K-edge in fluorescence mode using a Si (1 1 1) double-crystal monochromator at the beam line 10C at Pohang Light Source (PLS-II) in Korea. Electronic conductivity was determined using a Powder Resistivity Measurement System with a HPRM-M2 (Hantech, Korea).

3. RESULTS AND DISCUSSION

Figure 1(a) shows the XRD patterns of Li₂Fe_{1-x}Ru_xP₂O₇ ($x = 0, 0.005, 0.01, 0.02, 0.03, \text{ and } 0.04$). The diffraction patterns are in good agreement with the monoclinic structure, with a space group of P21/c observed for space group number 14 (ICSD collection code 236281). Ruthenium doped samples all exhibited similar XRD patterns, and it was observed that the monoclinic structure was unchanged after ruthenium doping. In order to characterize the fine structure of the samples, the diffraction patterns of Li₂Fe_{0.99}Ru_{0.01}P₂O₇ were subjected to Rietveld refinement using Fullprof software, the results of which are shown in Figure 1(b). The calculated lattice parameters for Li₂Fe_{1-x}Ru_xP₂O₇ ($x = 0, 0.005, 0.01, 0.02, 0.03, \text{ and } 0.04$) are shown in Table 1, including a reasonable fit indicator (*S*) range under 1.7, which was calculated by R_{wp}/R_{exp} .

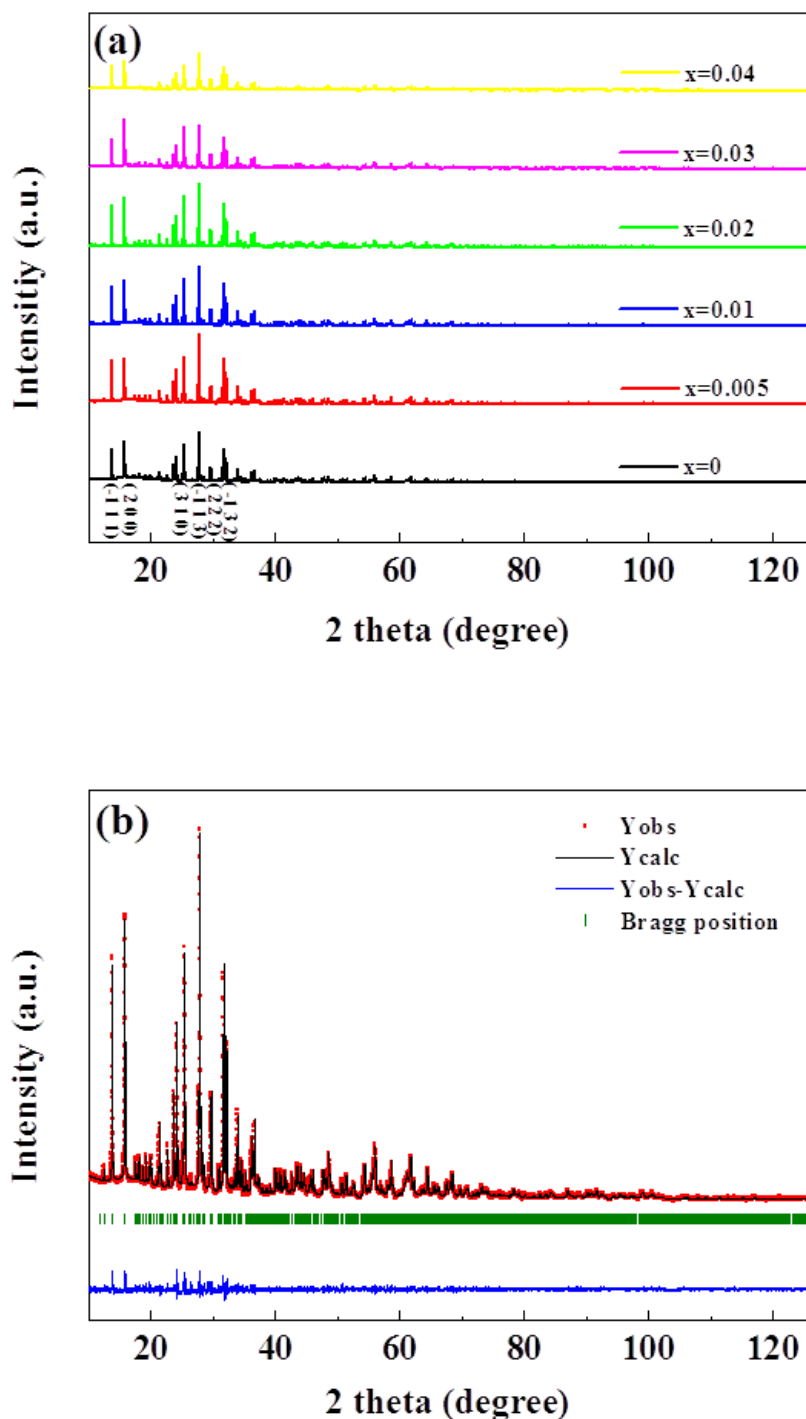
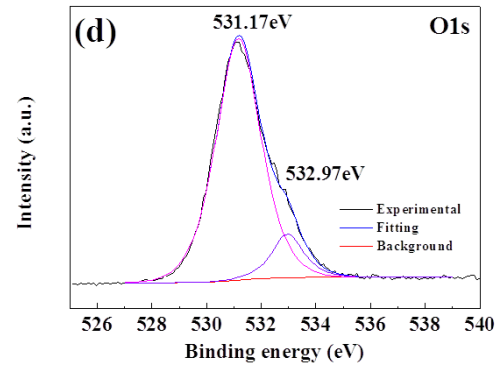
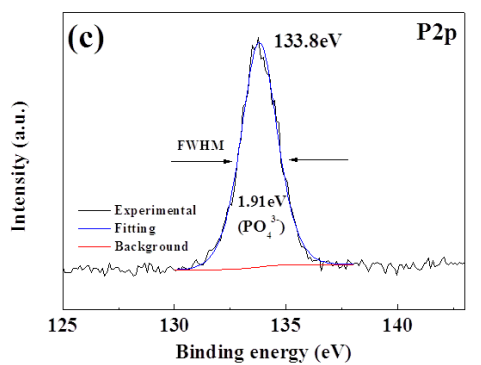
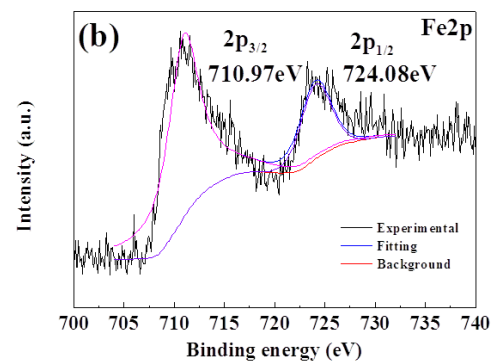
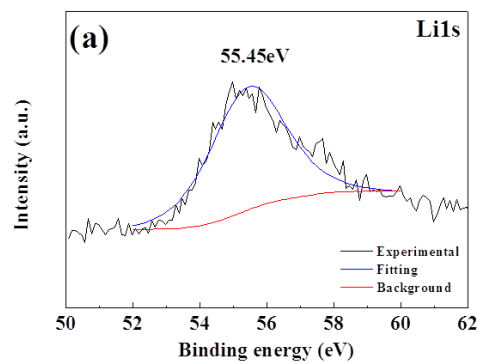


Figure 1. (a) XRD peaks of $\text{Li}_2\text{Fe}_{1-x}\text{Ru}_x\text{P}_2\text{O}_7$ ($x = 0, 0.005, 0.01, 0.02, 0.03,$ and 0.04), and (b) rietveld refinement data of $\text{Li}_2\text{Fe}_{0.99}\text{Ru}_{0.01}\text{P}_2\text{O}_7$.

The well-defined parameters indicate that ruthenium is well-substituted into the lattice of $\text{Li}_2\text{FeP}_2\text{O}_7$. There was a slight decrease in the lattice parameters of c and cell volume with increasing ruthenium substitution, which is likely due to the substitution of Fe^{2+} (0.78\AA) by the smaller radius Ru^{3+} (0.68\AA).

Table 1. Lattice parameters of $\text{Li}_2\text{Fe}_{1-x}\text{Ru}_x\text{P}_2\text{O}_7$ ($x = 0, 0.005, 0.01, 0.02, 0.03, \text{ and } 0.04$).

	a (Å)	b (Å)	c (Å)	β	V (Å ³)	S
x = 0	11.0246	9.7601	9.8129	101.554	1034.4828	1.56
x = 0.005	11.0243	9.7603	9.8128	101.554	1034.4596	1.31
x = 0.010	11.0247	9.7601	9.8124	101.549	1034.4587	1.51
x = 0.020	11.0239	9.7601	9.8126	101.549	1034.3970	1.50
x = 0.030	11.0244	9.7600	9.8118	101.548	1034.3673	1.55
x = 0.040	11.0228	9.7618	9.8076	101.528	1034.0341	1.50



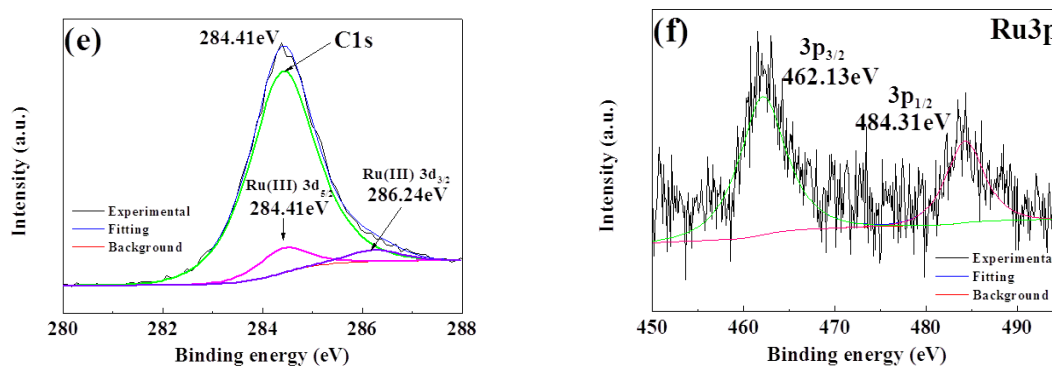
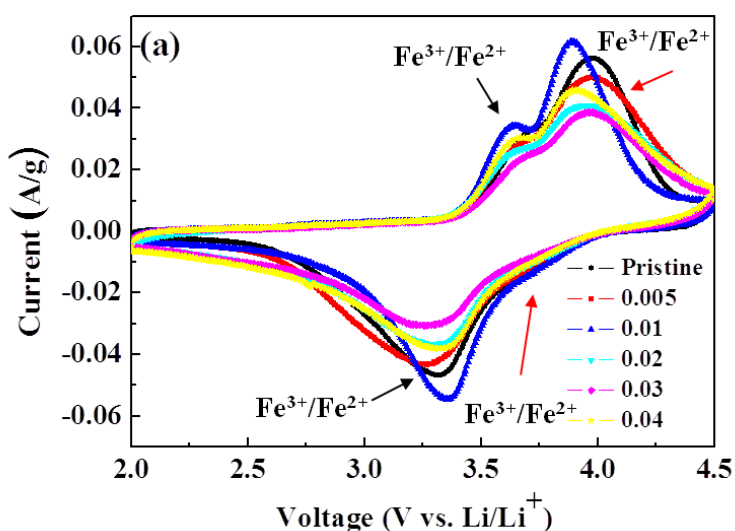


Figure 2. XPS spectra of Li₂FeP₂O₇: (a) Li1s, (b) Fe2p, (c) P2p, (d) O1s and Li₂Fe_{0.99}Ru_{0.01}P₂O₇: (e) C1s, Ru3d_{5/2}, Ru3d_{3/2}, (f) Ru3p_{3/2}, Ru3p_{1/2}.

To further confirm the oxidation and chemical states of elements within the samples, XPS spectra of each element are presented in Figure 2. The spectra in figures 2(a) to (d) show prominent bands of Li1s, Fe2p, P2p, and O1s within Li₂FeP₂O₇, while the spectra in 2 (e) and (f) show C1s, Ru3d_{5/2}, Ru3d_{3/2}, and Ru3p_{3/2}, Ru3p_{1/2} within the Li₂Fe_{0.99}Ru_{0.01}P₂O₇ sample. The XPS peak of Li1s at 55.45eV indicates the presence of monovalent Li⁺ in Li₂FeP₂O₇ [20, 26]. The XPS peaks of Fe2p have two prominent peaks, with the major peak at around 710.97 eV and the satellite peak at 724.08 eV, which can be assigned to Fe2p_{3/2} and Fe2p_{1/2}, respectively, indicating that the oxidation state of Fe is +2, which is in accordance with literature values [21]. The two overlapping oxygen peaks confirm the existence of terminal (531.17eV) and bridging (532.97eV) oxygen bonds in the P₂O₇ diphosphate polyhedral unit. The XPS spectra of Ru3d_{5/2}, and Ru3d_{3/2} show two prominent bands at 284.41eV and 286.24eV, which are in agreement with the literature vales for ruthenium (III) chloride [25, 26]. The less intense XPS peaks of Ru3p_{3/2} and Ru3p_{1/2} at 462.13eV and 484.31eV, which are reference peaks for Ru3p in ruthenium (III) chloride, are evidence of ruthenium doping in Li₂Fe_{0.99}Ru_{0.01}P₂O₇.



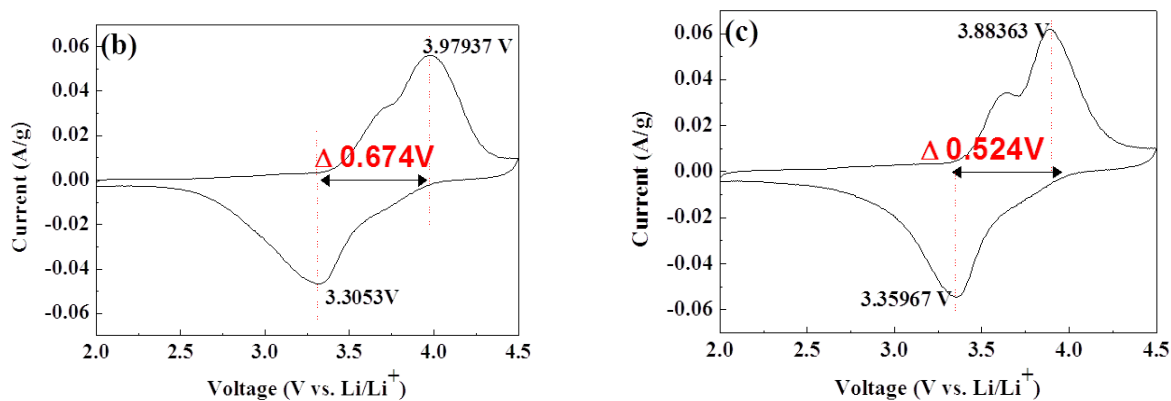


Figure 3. Cyclic voltammograms of (a) $\text{Li}_2\text{Fe}_{1-x}\text{Ru}_x\text{P}_2\text{O}_7$ ($x = 0, 0.005, 0.01, 0.02, 0.03,$ and 0.04) and polarization redox couple ($\text{Fe}^{2+}/\text{Fe}^{3+}$) of (b) $\text{Li}_2\text{FeP}_2\text{O}_7$, (c) $\text{Li}_2\text{Fe}_{0.99}\text{Ru}_{0.01}\text{P}_2\text{O}_7$.

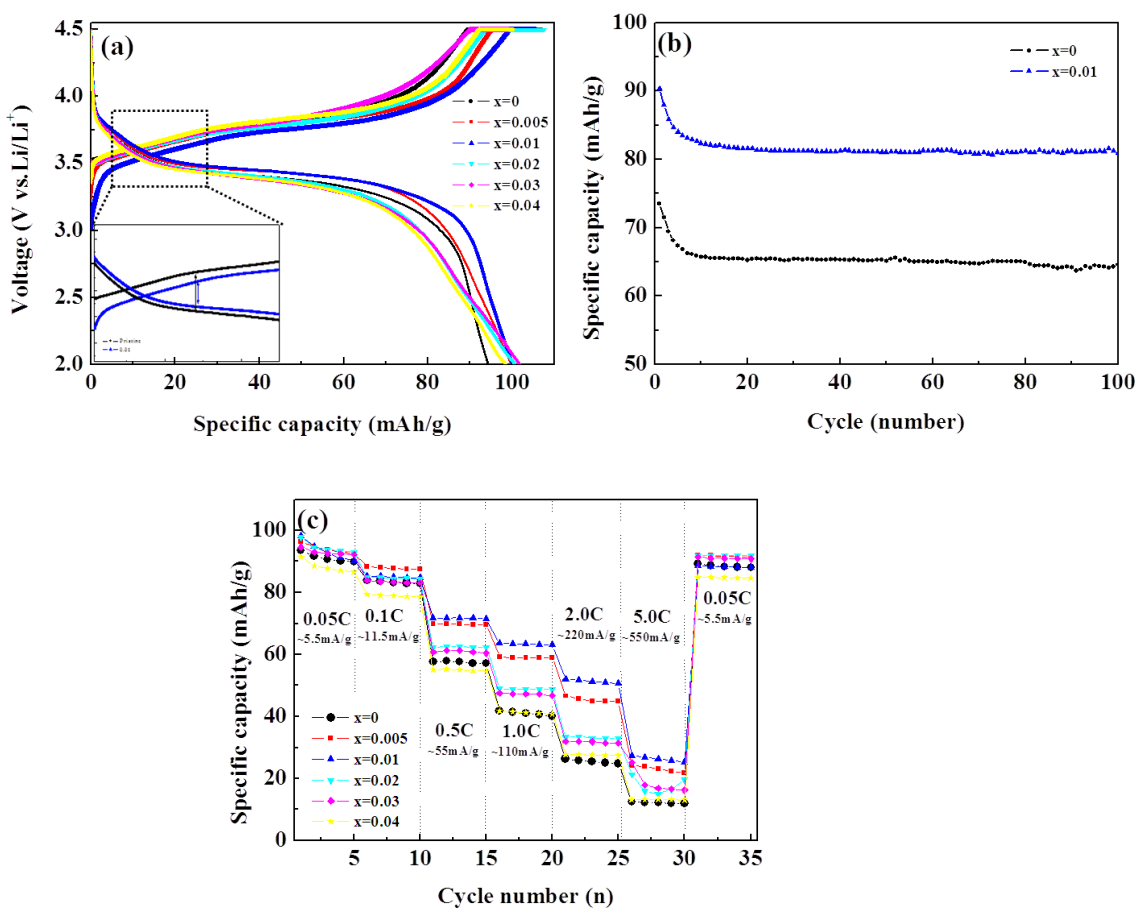


Figure 4. (a) The 1st CC/CV charge-discharge curves of $\text{Li}_2\text{Fe}_{1-x}\text{Ru}_x\text{P}_2\text{O}_7$ ($x = 0, 0.005, 0.01, 0.02, 0.03,$ and 0.04) at 0.05C ($\sim 5.5\text{mAh/g}$) and the magnification of the polarization of redox couple, and (b) cycle ability of $\text{Li}_2\text{Fe}_{1-x}\text{Ru}_x\text{P}_2\text{O}_7$ ($x = 0, 0.01$) at 0.2C ($\sim 22\text{mAh/g}$), and (c) rate-capability with the currents range from 0.05C ($\sim 5.5\text{mAh/g}$) to 5C ($\sim 550\text{mAh/g}$).

Table 2. Comparison the practical capacity of $\text{Li}_2\text{FeP}_2\text{O}_7$, LiFePO_4 , $\text{Li}_2\text{FeSiO}_4$, and LiFeBO_3 (mAh/g)

Material	Structure	Potential vs. Li/Li ⁺ (V)	Theoretical Capacity (mAh)	Practical Capacity (mAh)	R (%)	Ref.
$\text{Li}_2\text{FeP}_2\text{O}_7$	Monoclinic	3.5 (one-e)	110 (one-e)	94.405 (5.5 mA/g, 0.05C)	85.82	3
		4.5 (two-e)	220 (two-e)	-	-	
$\text{Li}_2\text{Fe}_{0.99}\text{Ru}_{0.01}\text{P}_2\text{O}_7$	-	-	110	100.217 (5.5 mA/g, 0.05C)	91.10	
LiFePO_4	Olivine	3.4	170	130 (2.0 mA/g,)	76.47	22
$\text{Li}_2\text{FeSiO}_4$	Tetrahedral	2.8	330	160 (-)	48.48	23
LiFeBO_3	Monoclinic	2.8	220	130 (0.05C)	59.09	24

Figure 3(a) shows the cyclic voltammograms of $\text{Li}_2\text{Fe}_{1-x}\text{Ru}_x\text{P}_2\text{O}_7$ ($x = 0, 0.005, 0.01, 0.02, 0.03,$ and 0.04) at the voltage range of 2.0~4.5V in the 1st cycle at 0.05C (~5.5mAh/g). It can be seen that there are two oxidation peaks and two reduction peaks which represent $\text{Fe}^{2+}/\text{Fe}^{3+}$ redox couple [27]. The reason is that these two voltage regions correspond to a preferential oxidation of different iron sites in $\text{Li}_2\text{FeP}_2\text{O}_7$, since iron has two different coordination numbers in the crystal structure: FeO_5 and FeO_6 . Polarization of the $\text{Fe}^{2+}/\text{Fe}^{3+}$ redox couple can be seen in Figures 3(b-c). The differences in voltage between oxidation and reduction peaks of $\text{Li}_2\text{FeP}_2\text{O}_7$ and $\text{Li}_2\text{Fe}_{0.99}\text{Ru}_{0.01}\text{P}_2\text{O}_7$ are $\Delta 0.674\text{V}$ and $\Delta 0.524\text{V}$, respectively. It can be seen in Figure 3(c) that $\text{Li}_2\text{Fe}_{0.99}\text{Ru}_{0.01}\text{P}_2\text{O}_7$ exhibits less polarization than $\text{Li}_2\text{FeP}_2\text{O}_7$ (Figure 3(b)). Also, the CV curves of $\text{Li}_2\text{Fe}_{0.99}\text{Ru}_{0.01}\text{P}_2\text{O}_7$ are sharper than those of $\text{Li}_2\text{FeP}_2\text{O}_7$ due to the more rapid insertion/extraction of Li^+ ions.

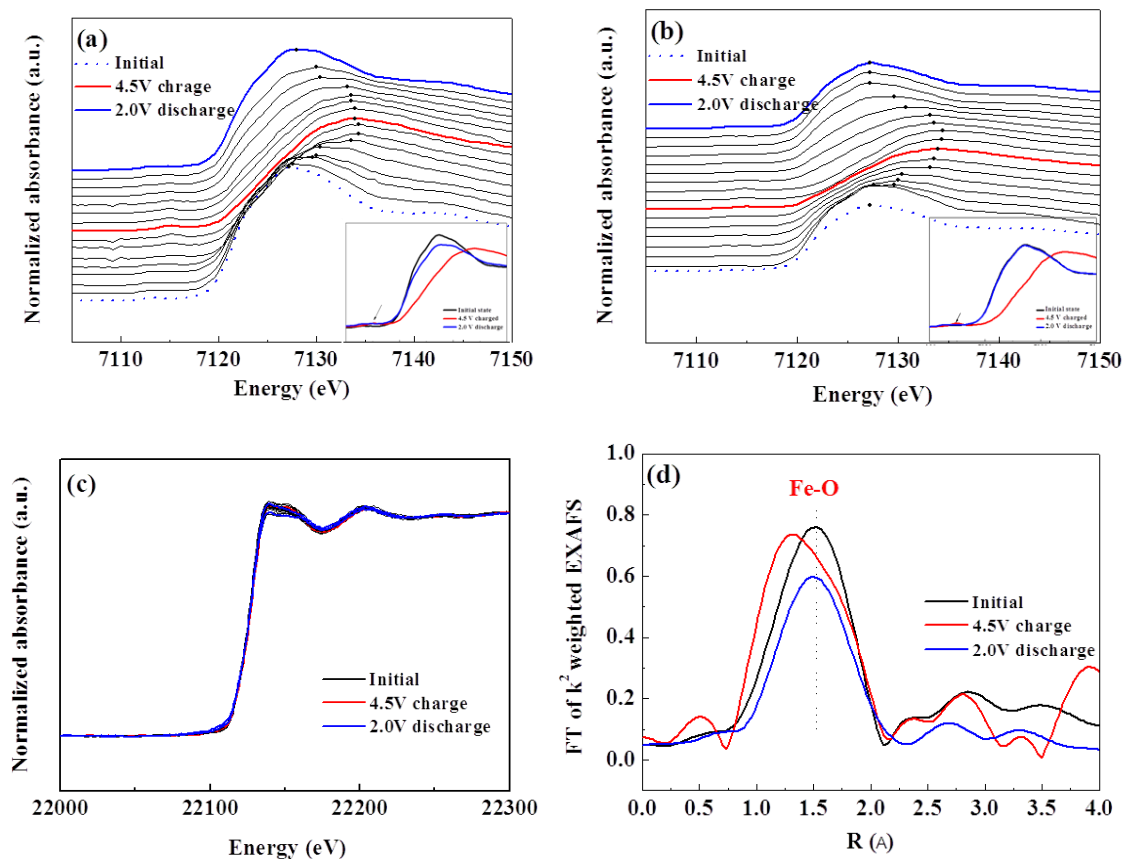
The initial CC/CV charge-discharge curves of $\text{Li}_2\text{Fe}_{1-x}\text{Ru}_x\text{P}_2\text{O}_7$ ($x = 0, 0.005, 0.01, 0.02, 0.03,$ and 0.04) were galvanostatically cycled at the voltage range of 2.0~4.5V at 0.05C (~5.5mAh/g) rate, with a constant voltage relaxation down to C/200 being applied once charging was complete, as shown in Figure 4(a). The 1st specific discharge capacities of CC/CV charge-discharge mode of $\text{Li}_2\text{Fe}_{1-x}\text{Ru}_x\text{P}_2\text{O}_7$ ($x = 0, 0.005, 0.01, 0.02, 0.03,$ and 0.04) at 0.05C (~5.5mAh/g) were 94.4052, 99.8702, 100.217, 100.642, 101.779, and 98.513mAh/g, respectively. These results show increasing specific capacity with increased ruthenium doping up to a content of 3%. $\text{Li}_2\text{Fe}_{0.99}\text{Ru}_{0.01}\text{P}_2\text{O}_7$ has the lowest polarization during electrochemical reaction, which is in agreement with cyclic voltammetry data (Figure 3). The cycling performances of $\text{Li}_2\text{FeP}_2\text{O}_7$ and $\text{Li}_2\text{Fe}_{0.99}\text{Ru}_{0.01}\text{P}_2\text{O}_7$ with a current density 0.2C (~22mAh/g) are shown in Figure 4(b). The capacity retention rates of $\text{Li}_2\text{FeP}_2\text{O}_7$ and $\text{Li}_2\text{Fe}_{0.99}\text{Ru}_{0.01}\text{P}_2\text{O}_7$ upon the 100th cycle were 87.83, and 89.62%, respectively. $\text{Li}_2\text{Fe}_{0.99}\text{Ru}_{0.01}\text{P}_2\text{O}_7$ had a slightly greater tendency to sustain a high discharge capacity than $\text{Li}_2\text{FeP}_2\text{O}_7$.

$\text{Li}_2\text{FeP}_2\text{O}_7$ compares with the iron based polyanion cathode materials such as LiFePO_4 , $\text{Li}_2\text{FeSiO}_4$, and LiFeBO_3 . The 1st practical capacity of $\text{Li}_2\text{FeP}_2\text{O}_7$, LiFePO_4 , $\text{Li}_2\text{FeSiO}_4$, and LiFeBO_3 has 94.405mAh/g, 130mAh/g [22], 160mAh/g [23], and 130mAh/g [24]. When the retention ratios were obtained through the theoretical capacity and the practical capacity, there have obtained 85.82%,

76.47%, 48.48%, and 59.09% at Table 2, respectively. $\text{Li}_2\text{FeP}_2\text{O}_7$ showed higher values than other materials. In addition, the retention ratio of $\text{Li}_2\text{Fe}_{0.99}\text{Ru}_{0.01}\text{P}_2\text{O}_7$ was 91.1%, which is higher than that of $\text{Li}_2\text{FeP}_2\text{O}_7$ [22-24].

The rate capabilities of $\text{Li}_2\text{Fe}_{1-x}\text{Ru}_x\text{P}_2\text{O}_7$ are shown in Figure 4(c). Coin-type cells were tested in the voltage range of 2.0~4.5V with a current range from 0.05C (~5.5mAh/g) to 5C (~550mAh/g) at room temperature. When the C-rate was increased, a decrease in specific discharge capacity was observed for all samples. However, $\text{Li}_2\text{Fe}_{0.99}\text{Ru}_{0.01}\text{P}_2\text{O}_7$ demonstrated a remarkably high rate-capability from 0.5C to 5C as compared with $\text{Li}_2\text{FeP}_2\text{O}_7$ and other ruthenium doped samples.

Figures 5(a-c) show the near edge spectra (XANES) of *in situ* XAS with galvanostatic charging for the 1st cycle between 2.0~4.5V (vs Li/Li⁺) at 0.2 C (~22mA/g) with a constant voltage at 4.5V for 2h. The spectra at the Fe K-edge were obtained in the transmission mode, while the Ru K-edge spectra were obtained in the fluorescence mode. Pre-edge peaks were magnified to confirm the iron oxidation states as well as the iron short range order for samples of $\text{Li}_2\text{FeP}_2\text{O}_7$ and $\text{Li}_2\text{Fe}_{0.99}\text{Ru}_{0.01}\text{P}_2\text{O}_7$. The Fe K-edge energy of $\text{Li}_2\text{Fe}_{0.99}\text{Ru}_{0.01}\text{P}_2\text{O}_7$ is shifted to the higher energy of Fe^{3+} (7134.4eV) at 4.5V while charging, and is shifted further towards the lower energy (7127.2eV) during the discharge process than that of $\text{Li}_2\text{FeP}_2\text{O}_7$ (7127.99eV) at 2.0V. $\text{Li}_2\text{Fe}_{0.99}\text{Ru}_{0.01}\text{P}_2\text{O}_7$ was found to retain its original oxidation states and local structure to a greater extent than $\text{Li}_2\text{FeP}_2\text{O}_7$. After the 1st cycle the XANES and 2.0V discharged XANES spectra are clearly overlapped in the case of $\text{Li}_2\text{Fe}_{0.99}\text{Ru}_{0.01}\text{P}_2\text{O}_7$. These results indicate that $\text{Li}_2\text{Fe}_{0.99}\text{Ru}_{0.01}\text{P}_2\text{O}_7$ has a highly stable structure during electrochemical reaction, undergoing fully reversible reactions and sustaining its original local structure.



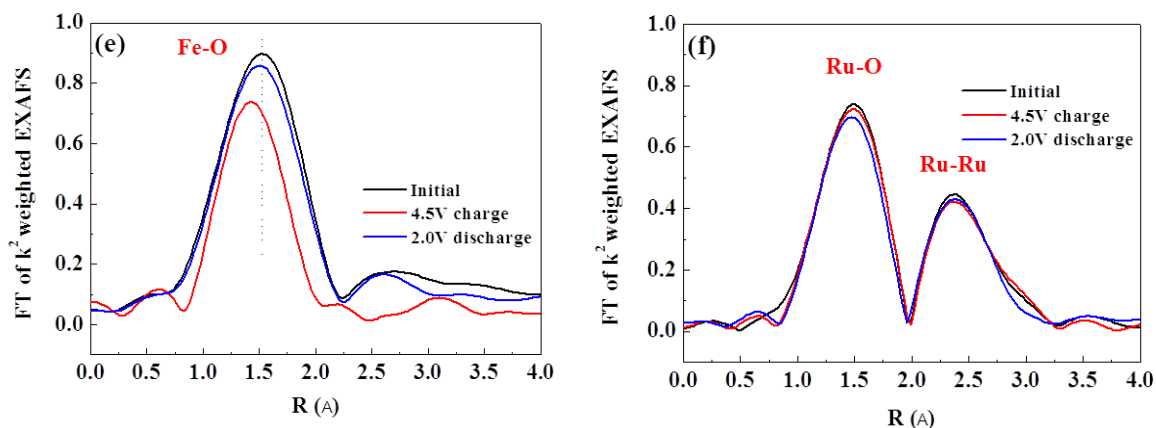
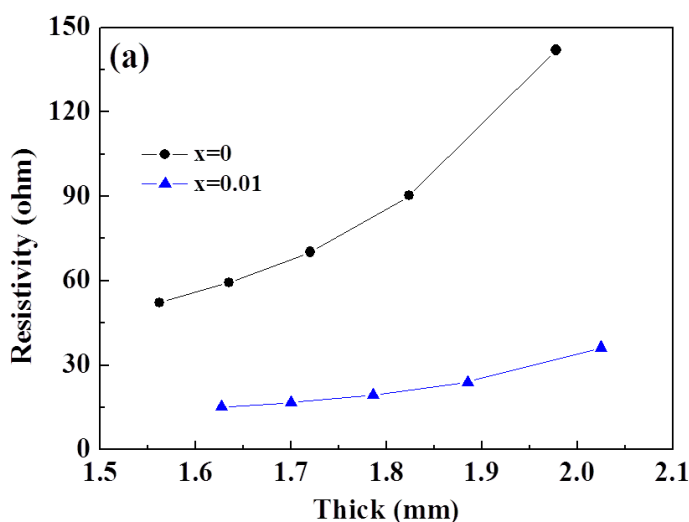


Figure 5. In-situ XAS spectra of Fe K-edge: (a) $\text{Li}_2\text{FeP}_2\text{O}_7$, (b) $\text{Li}_2\text{Fe}_{0.99}\text{Ru}_{0.01}\text{P}_2\text{O}_7$ and (c) in-situ XAS spectra of $\text{Li}_2\text{Fe}_{0.99}\text{Ru}_{0.01}\text{P}_2\text{O}_7$ Ru K-edge at 0.2C, and the k^2 -weighted Fourier transforms magnitude EXAFS spectra of Fe K-edge: (d) $\text{Li}_2\text{FeP}_2\text{O}_7$, (e) $\text{Li}_2\text{Fe}_{0.99}\text{Ru}_{0.01}\text{P}_2\text{O}_7$, and Ru K-edge of (f) $\text{Li}_2\text{Fe}_{0.99}\text{Ru}_{0.01}\text{P}_2\text{O}_7$.

The Ru K-edge was found to retain its local structure and initial absorption edges, which indicates stable oxidation states of ruthenium within $\text{Li}_2\text{Fe}_{0.99}\text{Ru}_{0.01}\text{P}_2\text{O}_7$. Ru^{3+} does not take part in the electrochemical reaction, but acts as a pillar to prevent the collapse of the local structure.

Figures 5(d-f) shows the k^2 -weighted Fourier transform magnitude EXAFS spectra. The first coordination shell consists of oxygen and the second consists of each transition metal [40]. The Fe-O (first shell) bond length undergoes substantial change during charge (4.5V) and discharge (2.0V) in the case of $\text{Li}_2\text{FeP}_2\text{O}_7$, as shown in Figure 5(d), but remains mostly unchanged during charge (4.5V) and discharge (2.0V) in the case of $\text{Li}_2\text{Fe}_{0.99}\text{Ru}_{0.01}\text{P}_2\text{O}_7$, as shown in Figure 5(e).



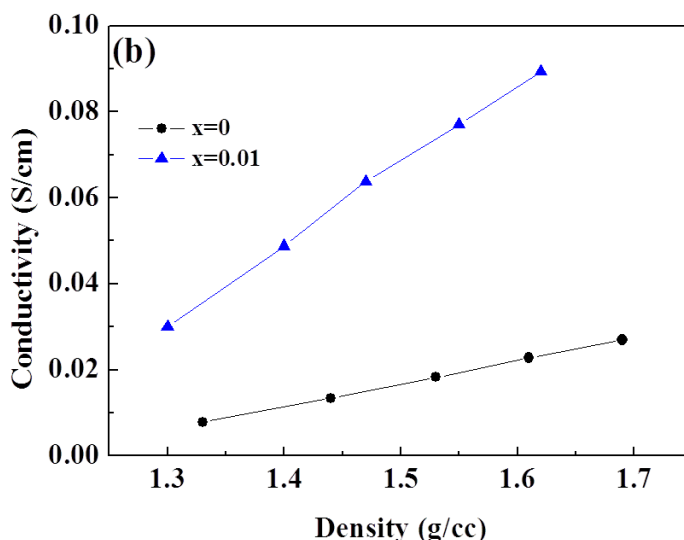
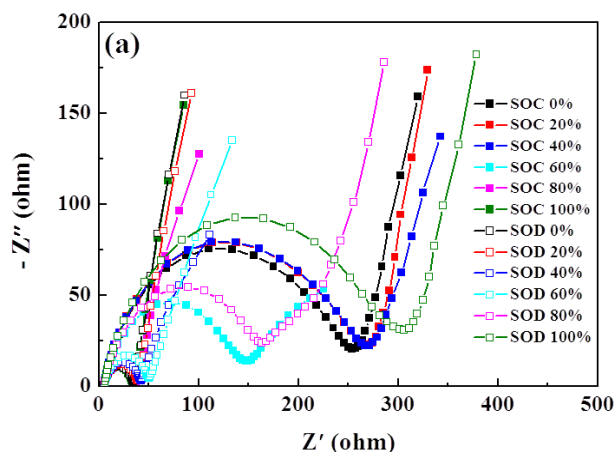


Figure 6. (a) Powder resistivity and (b) electronic conductivity of $\text{Li}_2\text{FeP}_2\text{O}_7$ and $\text{Li}_2\text{Fe}_{0.99}\text{Ru}_{0.01}\text{P}_2\text{O}_7$.

These results are indicative of the pillar effect of Ru^{3+} (0.68\AA) doping in Fe^{2+} (0.78\AA) sites, which can reduce volume change. In the case of $\text{Li}_2\text{FeP}_2\text{O}_7$, the cell volume changes as Fe^{2+} (0.78\AA) is oxidized to Fe^{3+} (0.65\AA) through electrochemical reaction. Figure 5(f) exhibits Ru-O (first shell) and Ru-Ru (second shell) bonds which demonstrate ruthenium doping within the lattice. The bond distances of both Ru-O and Ru-Ru do not change during electrochemical reaction.

Figure 6 illustrates the powder resistivity (a) and electronic conductivity (b) of $\text{Li}_2\text{FeP}_2\text{O}_7$ and $\text{Li}_2\text{Fe}_{0.99}\text{Ru}_{0.01}\text{P}_2\text{O}_7$. $\text{Li}_2\text{Fe}_{0.99}\text{Ru}_{0.01}\text{P}_2\text{O}_7$ has a lower powder resistivity and higher electronic conductivity than $\text{Li}_2\text{FeP}_2\text{O}_7$. In comparison with 3d orbitals of iron, the 4d orbitals of transition metals, such as ruthenium, with a larger radius overlap with the oxygen 2p orbitals to form wider conduction bands, facilitating the transfer of electrons from HOMO to LUMO during electrochemical reaction [28, 29].



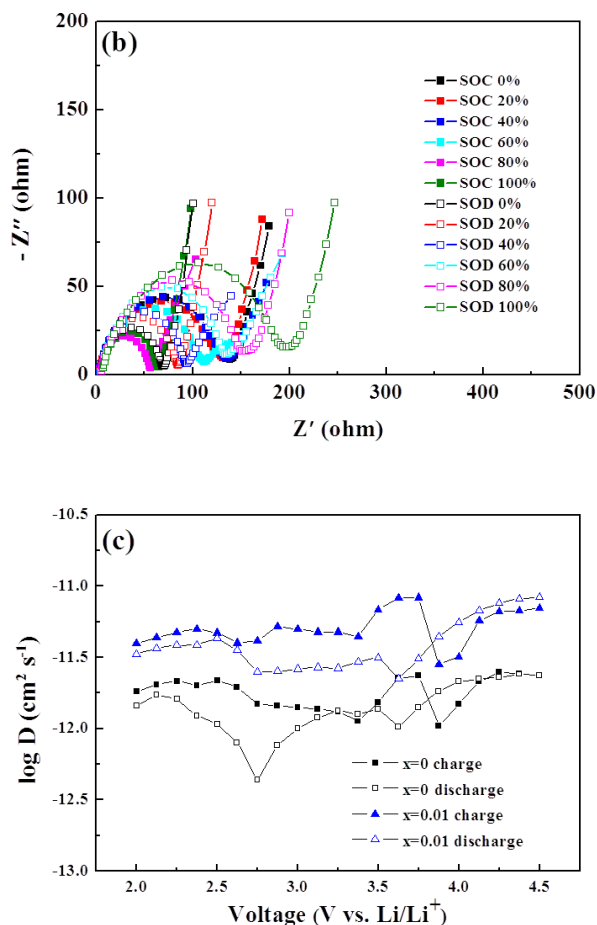


Figure 7. Nyquist plots at different voltages of SOC and SOD states of (a) $\text{Li}_2\text{FeP}_2\text{O}_7$ and (b) $\text{Li}_2\text{Fe}_{0.99}\text{Ru}_{0.01}\text{P}_2\text{O}_7$ in the voltage range of 2.0 to 4.5V and (c) the log plot of Li^+ diffusion coefficients (D_{Li^+}) calculated from the EIS data.

Figures 7(a) and (b) show Nyquist plots at different states of charge (SOC) and states of discharge (SOD) for samples of $\text{Li}_2\text{FeP}_2\text{O}_7$ and $\text{Li}_2\text{Fe}_{0.99}\text{Ru}_{0.01}\text{P}_2\text{O}_7$. Electrochemical impedance spectra (EIS) were recorded in the voltage range of 2.0-4.5V. EIS is a useful method to demonstrate the kinetic behavior of lithium ions. Figures 7(a) and (b), representing (a) $\text{Li}_2\text{FeP}_2\text{O}_7$, and (b) $\text{Li}_2\text{Fe}_{0.99}\text{Ru}_{0.01}\text{P}_2\text{O}_7$, demonstrate a clear semicircle in the high-frequency range and a straight line with an inclined slope, which is attributed to Warburg diffusion impedance (Z_w). The semicircle indicates the charge transfer process (R_{ct}), and it was observed that $\text{Li}_2\text{Fe}_{0.99}\text{Ru}_{0.01}\text{P}_2\text{O}_7$ exhibits a lower R_{ct} value during electrochemical reaction. Figure 7(c) shows the Li^+ diffusion coefficients (D_{Li^+}) calculated from the EIS data during both charge and discharge processes. The D_{Li^+} vs. voltage of charge processes has two minima near 3.375V and 3.875V, which corresponding to the two main redox processes observed through cyclic voltammetry of both $\text{Li}_2\text{FeP}_2\text{O}_7$ and $\text{Li}_2\text{Fe}_{0.99}\text{Ru}_{0.01}\text{P}_2\text{O}_7$ (Figure 3). The lithium diffusion coefficients of $\text{Li}_2\text{Fe}_{0.99}\text{Ru}_{0.01}\text{P}_2\text{O}_7$ were in the range of 2.82×10^{-9} to $8.31 \times 10^{-10} \text{ cm}^2 \text{ s}^{-1}$ during charge and 2.24×10^{-10} to $8.39 \times 10^{-10} \text{ cm}^2 \text{ s}^{-1}$ during discharge, higher than those of $\text{Li}_2\text{FeP}_2\text{O}_7$, as shown in Table 3.

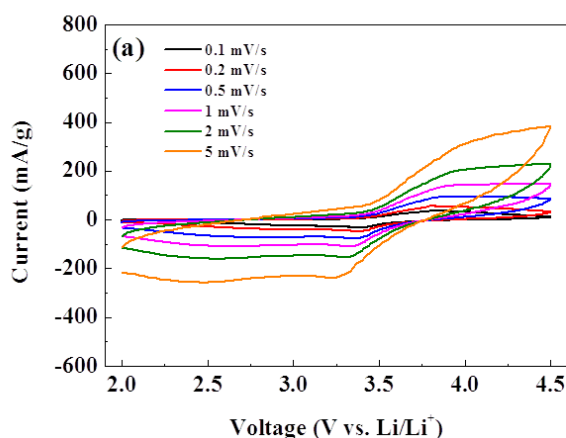
Table 3. The Li^+ diffusion coefficients (D_{Li^+}) calculated from the EIS data of $\text{Li}_2\text{FeP}_2\text{O}_7$ and $\text{Li}_2\text{Fe}_{0.99}\text{Ru}_{0.01}\text{P}_2\text{O}_7$.

Sample	Voltage (V vs. Li/Li^+)	D_{Li^+} (cm^2/s)
$\text{Li}_2\text{FeP}_2\text{O}_7$	2.0 – 4.5V (charge)	1.04×10^{-12} - 2.50×10^{-12}
	4.5 – 2.0V (discharge)	1.00×10^{-10} - 7.98×10^{-10}
$\text{Li}_2\text{Fe}_{0.99}\text{Ru}_{0.01}\text{P}_2\text{O}_7$	2.0 – 4.5V (charge)	2.82×10^{-9} - 8.31×10^{-10}
	4.5 – 2.0V (discharge)	2.24×10^{-10} - 8.39×10^{-10}

Figure 8 shows cyclic voltammograms of (a) $\text{Li}_2\text{FeP}_2\text{O}_7$ and (b) $\text{Li}_2\text{Fe}_{0.99}\text{Ru}_{0.01}\text{P}_2\text{O}_7$ with different scan rates of 0.1-5.0mV/s. As the scan rate is increased, the peak current also increases with a slight shift of the current peaks. $\text{Li}_2\text{Fe}_{0.99}\text{Ru}_{0.01}\text{P}_2\text{O}_7$ exhibited a faster (de)-lithiation electrochemical reaction compared to that of $\text{Li}_2\text{FeP}_2\text{O}_7$. As shown in Figure 8(c), there exists a linear relationship between the peak current and the square root of scan rate.

Table 4. Calculated D_{Li^+} values of $\text{Li}_2\text{FeP}_2\text{O}_7$ and $\text{Li}_2\text{Fe}_{0.99}\text{Ru}_{0.01}\text{P}_2\text{O}_7$ obtained from CV results.

Sample	D_{Li^+} (cm^2s^{-1})	Scan rate (mV/s)					
		0.1	0.2	0.5	1.0	2.0	5.0
$\text{Li}_2\text{FeP}_2\text{O}_7$	C	3.09×10^{-10}	4.27×10^{-10}	5.34×10^{-10}	4.51×10^{-10}	4.92×10^{-10}	5.41×10^{-10}
	D	2.39×10^{-10}	2.80×10^{-10}	3.58×10^{-10}	2.90×10^{-10}	2.92×10^{-10}	2.80×10^{-10}
$\text{Li}_2\text{Fe}_{0.99}\text{Ru}_{0.01}\text{P}_2\text{O}_7$	C	5.77×10^{-10}	8.54×10^{-10}	1.44×10^{-9}	1.35×10^{-9}	1.51×10^{-9}	1.42×10^{-9}
	D	5.01×10^{-10}	6.52×10^{-10}	9.81×10^{-10}	9.17×10^{-10}	9.16×10^{-10}	7.80×10^{-10}



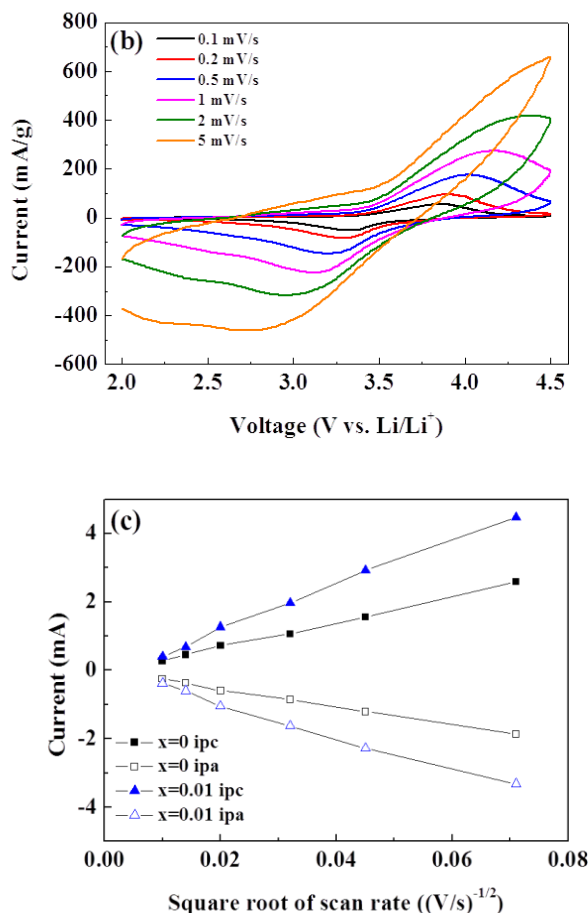


Figure 8. Cyclic voltammograms of (a) $\text{Li}_2\text{FeP}_2\text{O}_7$ and (b) $\text{Li}_2\text{Fe}_{0.99}\text{Ru}_{0.01}\text{P}_2\text{O}_7$ with different scan rates and (c) the linear relationship between the peak current and the square root of scan rate of $\text{Li}_2\text{FeP}_2\text{O}_7$ and $\text{Li}_2\text{Fe}_{0.99}\text{Ru}_{0.01}\text{P}_2\text{O}_7$.

Table 4 contains calculated D_{Li^+} values for $\text{Li}_2\text{FeP}_2\text{O}_7$ and $\text{Li}_2\text{Fe}_{0.99}\text{Ru}_{0.01}\text{P}_2\text{O}_7$, as obtained from CV results in Figure 8(a) and (b). The diffusion coefficient of lithium ions can be determined by using the Randles-Sevcik equation. The lithium ion diffusion coefficient values for $\text{Li}_2\text{Fe}_{0.99}\text{Ru}_{0.01}\text{P}_2\text{O}_7$ were in the range of 1.35×10^{-9} – $8.54 \times 10^{-10} \text{ cm}^2 \text{ s}^{-1}$ during charge and 5.01×10^{-10} – $9.81 \times 10^{-10} \text{ cm}^2 \text{ s}^{-1}$ during discharge, which are slightly higher than those of $\text{Li}_2\text{FeP}_2\text{O}_7$.

$\text{Li}_2\text{Fe}_{0.99}\text{Ru}_{0.01}\text{P}_2\text{O}_7$ was found to exhibit the highest electrical conductivity and ionic conductivity of all tested samples in this study. Partial substitutions of iron by ruthenium greatly stabilize the structure and improve the cycling behavior of the electrodes. Therefore, the higher electrochemical performance of $\text{Li}_2\text{Fe}_{0.99}\text{Ru}_{0.01}\text{P}_2\text{O}_7$ was related with structure stability and electronic conductivity and ionic diffusion coefficient.

4. CONCLUSIONS

Monoclinic $\text{Li}_2\text{Fe}_{1-x}\text{Ru}_x\text{P}_2\text{O}_7$ ($x = 0, 0.005, 0.01, 0.02, 0.03, \text{ and } 0.04$) were prepared via a sol-gel synthesis. The pillar effect of Ru^{3+} doping was determined using *in situ* XAS. It was found that

Ru^{3+} in the lattice acts as a pillar to prevent the collapse of the crystal structure during electrochemical reaction. The specific discharge capacities were found to increase after ruthenium doping to the tune of 3%. Notably, $\text{Li}_2\text{Fe}_{0.99}\text{Ru}_{0.01}\text{P}_2\text{O}_7$ exhibited excellent rate capability and cycling performance during 100 cycles. $\text{Li}_2\text{Fe}_{0.99}\text{Ru}_{0.01}\text{P}_2\text{O}_7$ exhibited improved electronic and ionic conductivities as compared with $\text{Li}_2\text{FeP}_2\text{O}_7$. EIS and CV determinations were made in order to determine the D_{Li^+} as evidence for increased ionic conductivities in $\text{Li}_2\text{Fe}_{0.99}\text{Ru}_{0.01}\text{P}_2\text{O}_7$. $\text{Li}_2\text{Fe}_{0.99}\text{Ru}_{0.01}\text{P}_2\text{O}_7$ can effectively improve the electrochemical reaction kinetics of Li^+ intercalation/de-intercalation.

ACKNOWLEDGEMENTS

This work was supported by the Priority Research Centers Program through the National Research Foundation of Korea (NRF), funded by the Ministry of Education, Science and Technology (MEST) of the Korean government (2009-0093818).

References

1. F. Omenya, N.A. Chernova, R. Zhang, J. Fang, Y. Huang, F. Cohen, N. Dobrzynski, S. Senanayake, W. Xu, M.S., *Chemistry of Materials*, 25 (2012) 85.
2. L. Yuan, Z. Wang, W. Zhang, X. Hu, J. Chen, Y. Huang, J.B. Goodenough, *Energy and Environmental Science*, 4 (2011) 269.
3. A. Gutierrez, N.A. Benedek, A. Manthiram, *Chemistry of Materials*, 25 (2013) 4010.
4. N. Furuta, S. Nishimura, P. Barpanda, A. Yamada, *Chemistry of Materials*, 24 (2012) 1055.
5. S. Nishimura, M. Nakamura, R. Natsui, A. Yamada, *J. Am. Chem. Soc.*, 132 (2010) 13596.
6. N. Ravet, Y. Chouinard, J. Magnan, S. Besner, M. Gauthier, M. Armand, *J. Power Sources*, 97 (2001) 503.
7. A.A. Salah, A. Mauger, K. Zaghbi, J. Goodenough, N. Ravet, M. Gauthier, F. Gendron, C. Julien, *Journal of Electrochem. Soc.*, 153 (2006) A1692.
8. K. Zaghbi, K. Striebel, A. Guerfi, J. Shim, M. Armand, M. Gauthier, *Electrochim. Acta*, 50 (2004) 263.
9. A. Blidberg, L. Haggstrom, T. Ericsson, C. Tengstedt, T. Gustafsson, and F. Bjorefors, *Chemistry of Materials*, 27 (2015) 3801
10. J.M. Clark, S. Nishimura, A. Yamada, M.S. Islam, *Angewandte Chemie*, 124 (2012) 13326.
11. P. Barpanda, T. Ye, S. Chung, Y. Yamada, S. Nishimura, A. Yamada, *Journal of Materials Chemistry*, 22 (2012) 13455.
12. J. Du, L. Jiao, Q. Wu, Y. Liu, Y. Zhao, L. Guo, Y. Wang, H. Yuan, *Electrochim. Acta*, 103 (2013) 219.
13. M. Saito, S. Yano, T. Maekawa, A. Tasaka, M. Inaba, *ECS Transactions*, 50 (2013) 251.
14. H. Nagano, I. Taniguchi, *J. Power Sources*, 298 (2015) 280.
15. H. Jang, and I. Taniguchi, *J. Alloys and Compounds*, 709 (2017) 557.
16. J. Xu, S. Chou, Q. Gu, M.M. Din, H. Liu, S. Dou, *Electrochim. Acta*, 141 (2014) 195.
17. T. Ye, P. Barpanda, S. Nishimura, N. Furuta, S. Chung, A. Yamada, *Chemistry of Materials*, 25 (2013) 3623.
18. K. Horiba, S. Ito, S. Kurosumi, N. Nagamura, S. Toyoda, H. Kumigashira, M. Oshima, N. Furuta, S. Nishimura, A. Yamada, *Journal of physics : conference series*, 502 (2014) 012004.
19. J. Li, Y. Zhang, J. Li, L. Wang, X. He, J. Gao, *Ionics*, 17 (2011) 671.
20. H. Ota, Y. Sakata, X. Wang, J. Sasahara, *J. Electrochemical Society*, 151 (2004) A437.
21. A.M. Anderson, K. Edstrom, *J. Electrochemical Society*, 148 (2001) A1100.

22. A. K. Padhi, K. S. Nanjundaswamy, and J. B. Goodenough. *J. Electrochemical Society*, 144 (1997) 1188
23. A. Nyten, A. Abouimrane, M. Armand, T. Gustafsson, and J. O. Thomas. *Electrochemistry Communications*, 7 (2005) 156.
24. V. Legagneur, Y. An, A. Mosbah, R. Portal, A. Le Gal La Salle, A. Verbaere, and D. Guyomard. *Solid State Ionics*, 139 (2001) 37.
25. J.C. Dupin, D. Gonbeau, P. Vinatier, *Physical Chemistry Chemical Physics*, 2 (2000) 1319.
26. P. Kumar, B. Sain, S.L. Jain, *Journal of Materials Chemistry A*, 2 (2014) 11246.
27. B. Zhang, X. Ou, J. Zheng, L. Ming, Y. Han, J. Wang, S. Qin, *Electrochim. Acta*, 133 (2014) 1.
28. H. Wang, H. Xia, M.O. Lai, L. Lu, *Electrochemistry Communications*, 11 (2009) 1539.
29. H. Wang, T.A. Tan, P. Yang, M.O. Lai, L. Lu, *The Journal of Physical Chemistry C*, 115 (2011) 6102.

© 2018 The Authors. Published by ESG (www.electrochemsci.org). This article is an open access article distributed under the terms and conditions of the Creative Commons Attribution license (<http://creativecommons.org/licenses/by/4.0/>).